

See discussions, stats, and author profiles for this publication at: <https://www.researchgate.net/publication/215713380>

Determination of the Particle Size, Available Surface Area, and Nature of Exposed Sites for Silica–Alumina–Supported Pd Nanoparticles: A Multitechnical Approach

ARTICLE in THE JOURNAL OF PHYSICAL CHEMISTRY C · JUNE 2009

Impact Factor: 4.77 · DOI: 10.1021/jp9023712

CITATIONS

59

READS

51

8 AUTHORS, INCLUDING:



Riccardo Pellegrini

Chimet s.p.a.

14 PUBLICATIONS 231 CITATIONS

SEE PROFILE



Serena Bertarione

TitaC srl

50 PUBLICATIONS 767 CITATIONS

SEE PROFILE



A. Zecchina

Università degli Studi di Torino

560 PUBLICATIONS 19,882 CITATIONS

SEE PROFILE



Carlo Lamberti

Università degli Studi di Torino

379 PUBLICATIONS 13,086 CITATIONS

SEE PROFILE

Determination of the Particle Size, Available Surface Area, and Nature of Exposed Sites for Silica–Alumina-Supported Pd Nanoparticles: A Multitechnical Approach

G. Agostini,[†] R. Pellegrini,[‡] G. Leofanti,^{‡,§} L. Bertinetti,[†] S. Bertarione,[†] E. Groppo,^{*,†} A. Zecchina,[†] and C. Lamberti[†]

Dipartimento di Chimica IFM, INSTM centro di Riferimento and NIS Centre of Excellence, Università di Torino, Via P. Giuria 7, I-10125 Torino, Italy, Chimet SpA, Catalyst Division, Via di Pescaiola 74, Vicomaggio Arezzo, I-52041 Italy, and Consultant, Via Firenze 43, 20010 Canegrate (Milano), Italy

Received: March 17, 2009; Revised Manuscript Received: April 14, 2009

In this work we used several complementary techniques (TEM, TPR, CO chemisorption, EXAFS and FTIR spectroscopy) to understand the effects of the activation temperature and activation atmosphere (air or H₂) on the particle size distribution, the fraction, and the type of exposed surface sites of Pd nanoparticles supported on a high surface area SiO₂–Al₂O₃ (SA) support. Pd particle distribution has been carefully determined by a high statistic TEM study, from which the cuboctahedral-like shape of the metal particles is demonstrated. Assuming a model of perfect cuboctahedral particles, from the TEM particle size distribution we estimated the expected average Pd first shell coordination number. This value is slightly larger than that directly found by EXAFS owing to the fraction of very small Pd particles ($d < 6\text{--}8\text{ Å}$) that basically escape TEM detection. The same geometrical model allows prediction, from TEM particle size distribution, of the metal dispersion observed by CO chemisorption (S/V_{Chemi}). The S/V_{Chemi} value drops significantly upon increasing the H₂-reduction temperature. According to TEM, the sintering process can account only for a very small fraction of the S/V_{Chemi} decrease, suggesting an important poisoning of the potentially available Pd surface. This hypothesis is supported by a parallel experiment of thermal decomposition at the same temperature (in absence of H₂), showing a S/V_{Chemi} value almost unchanged. FTIR spectroscopy of adsorbed CO, probing the nature of the Pd surface available for adsorption, confirms the hypothesis.

1. Introduction

The catalytic properties of metal nanoparticles are a function of their available surface area, that in turns depends upon the particle size, the dispersion, and the presence/absence of poisoning and/or covering species. The identification of the relationship existing between catalyst's structure and catalytic activity/selectivity is the main goal in research applied to catalysis.^{1,2} It is clear that such a correlation can be understood only when a complete characterization of the active sites is achieved. This is not a trivial task when dealing with supported metal nanoparticles, because application of few characterization techniques usually gives only a partial view of the catalyst's properties. As an example, chemisorption of specific probes^{3,4} results in the determination of the fraction of surface metal atoms, but requires the assumption of the average probe/metal surface stoichiometry. EXAFS spectroscopy^{4–16} provides an estimation of the average particle size from the average first shell metal–metal coordination number N , but the particle morphology must be assumed in advance. Both techniques require a priori assumptions and result in an output that is a simple average value. TEM^{3,4,8,10,11,15–17} is more informative, as it provides both the particle morphology and the particle size distribution. However, an incorrect particle size distribution may be obtained, as very small particles preferentially escape detection, and the limited number of sampled particles may not

be representative of the overall distribution. On top of this, the three mentioned techniques fail in discriminating among the different surface sites. Probing the type of exposed surface sites is the goal of FTIR spectroscopy^{12,17–25} of adsorbed probe molecules, that however usually fails in providing quantitative numbers for the relative population of the different adsorbing sites, because of the difficulties in determining the extinction coefficients of the different IR bands. On these bases, it is evident that the use of a single technique alone cannot provide a complete picture of the properties of supported metal nanoparticles.

In this work we present a systematic and careful multitechnical approach to determine the particle size distribution, the fraction, and the type of exposed surface sites in the case of Pd nanoparticles supported on silica–alumina (hereafter SA). TEM, CO chemisorption, EXAFS, TPR, and FTIR spectroscopy of adsorbed CO are applied to investigate the properties of Pd/SA system as a function of the temperature (up to 823 K) and of the atmosphere (H₂ and air) used in the treatment procedure.

Other works in the literature concerning metal nanoparticles present a combination of TEM, EXAFS, and/or chemisorption data, where the average particle size $\langle d \rangle_{\text{TEM}}$ determined by TEM is compared with the average particle diameter estimated by EXAFS and/or with the surface/volume ratio obtained by chemisorption results. In this work we demonstrated that, by considering not just the average $\langle d \rangle_{\text{TEM}}$ value but the complete particle size distribution obtained by TEM, a much better agreement is obtained with both EXAFS and CO chemisorption results. Moreover, only a combination of TEM, CO chemisorption, and FTIR spectroscopy demonstrates the

* Corresponding author. E-mail: elena.groppo@unito.it; tel.: +39011-6707841; fax: +39011-6707855.

[†] Università di Torino.

[‡] Chimet SpA.

[§] Consultant.

TABLE 1: Adsorption of N₂ at 77 K on Pd/SA Catalyst Subjected to Different Thermal Treatments^a

	air			H ₂		
	393 K	673 K	823 K	393 K	673 K	823 K
A_s (m ² g ⁻¹)	141	125	124	143	125	125
V_p (mm ³ g ⁻¹)	827	719	716	844	728	721
D_m (Å)	235	230	231	237	233	231
c	151	127	110	153	131	116

^a The changes of surface area (A_s), pore volume (V_p), mean pore diameter (D_m), and parameter c of the BET equation as a function of atmosphere (air or H₂) and temperature of thermal treatment are reported.

occurrence of a poison phenomenon upon H₂-reduction at high temperature and advances the hypothesis on the nature of the poison.

The presented multitechnical approach has been applied here to metal-supported Pd nanoparticles that have relevance in the field of catalysis. Indeed, Pd nanoparticles supported on a large variety of systems (e.g., active carbons, oxides, polymers) exhibit good catalytic properties in hydrogenation reactions, making them widely used in fine chemical synthesis.^{26,27} However, this methodology represents a general approach that could be straightforwardly extended to the characterization of other metal nanoparticles that can play an important role in the design of advanced materials with new electrical,^{28–30} optical,^{28–32} and photochemical^{33,34} applications.

2. Experimental Section

2.1. Sample Preparation and Nomenclature. A sodium-neutralized silica–alumina (SA in the following) with a SiO₂/Al₂O₃ ratio of 5.7 has been used as support. Pd catalysts (Pd/SA in the following) were prepared by the deposition–precipitation method.^{35,36} Briefly, palladium hydroxide was deposited onto the support by using Na₂PdCl₄ as a palladium precursor and Na₂CO₃ as basic agent. The supported palladium hydroxide was then water-washed until residual chlorides were removed and dried at 393 K overnight. Final Pd/SA catalyst contains 2.05% Pd and some impurities arising from SA (Na 2.64%, K 0.04%, Ca 0.05%, Mg 0.04%, S 0.08%, as determined by XRF technique). It has a surface area of 141 m²/g and a pore volume of 0.83 cm³/g, as evaluated by N₂ adsorption measurements.³⁷

Supported metal particles are then obtained via the reduction of the precursor in hydrogen atmosphere. In order to follow the behavior of the metal particles, three reduction temperatures have been investigated: 393, 673, and 823 K. The evolution of the surface area and porosity of Pd/SA catalyst as a function of temperature and atmosphere of treatments has been followed in detail by adsorption of N₂ at 77 K and reported by us in a previous work.³⁷ Table 1 resumes the A_s , V_p , and D_m values under the conditions adopted in this work. It is evident that calcination in air up to 823 K causes very few changes in the morphology of the sample: a moderate decrease of A_s and V_p is observed, while the pore size (D_m) remains almost unchanged. This evolution has been associated with the loss of water. No significant differences between treatments in air and H₂ are observed.

2.2. Characterization Techniques. 2.2.1. TPR, TPD, and CO Chemisorption. Micromeritics Autochem 2910 instrument has been used for temperature-programmed reduction (TPR), temperature-programmed desorption (TPD), and CO chemisorption measurements. TPR has been carried out using a heating rate of 5 K min⁻¹ from 193 to 873 K in a 5% H₂ in Ar

mixture at a flow rate of 50 cm³min⁻¹. For TPD, the heating rate has been set to 5 K min⁻¹ from room temperature up to 1073 K in He carrier at a flow rate of 50 cm³ min⁻¹. In both cases, a molecular sieve trap has been put between the sample holder and the detector in order to adsorb water eventually released from the sample.

CO chemisorption experiments have been performed by the dynamic pulse method at 323 K. The catalyst was reduced in situ at 393 K with the following procedure: (i) the sample was loaded inside the U-tube, (ii) it was heated in He to 393 K (with a 10 K min⁻¹ heating rate), (iii) H₂ was fed for 30 min; (iv) the sample was finally cooled to 323 K in He (with a 10 K min⁻¹ heating rate), and (v) five CO pulses of known volume were injected into the sample under helium flow. The measurement was carried out by using catalysts dried at 393 K overnight. In order to determine the available surface Pd atoms (surface to volume ratio, S/V_{chemi}) a CO/Pd average stoichiometry = 1 was assumed. This assumption has been verified by a parallel series of measurements performed on three different samples treated at two different temperatures with H₂–O₂ static volumetric titration, that gives a O/Pd average stoichiometry close to 1.³⁸ The two methods/techniques give a CO/O ratio in the 0.94–1.13 range, that is a strong support for the assumption of a CO/Pd average stoichiometry = 1.

2.2.2. HRTEM. High-resolution transmission electron micrographs (HRTEM) were obtained with a JEOL 3010-UHR instrument operating at 300 kV, equipped with a 2k × 2k pixels Gatan US1000 CCD camera. Samples were deposited on a copper grid covered with a lacey carbon film. Particle size distributions were obtained, counting at least 200 particles. To present the data uniformly, a class width of 1 nm was chosen for all the particle size distributions. As the sample exhibited very small Pd particles, proper contrast/sampling conditions were set by (a) counting only Pd particles found on regions of the support thin enough to appreciate the smallest contrast differences and (b) acquiring images at a magnification of 400 k × (0.026 nm per pixel). However, it must be considered that particles with diameter below 1 nm might escape the detection by this technique.

For each particle size distribution the following values have been estimated: (a) the average particle diameter, $\langle d \rangle_{\text{TEM}}$; (b) the standard deviation, σ ; (c) the surface to volume ratio, S/V_{TEM} , representing the overall Pd surface sites, according to the procedure discussed in the following. We adopted the model of Fritsche et al.,³⁹ further developed by Montejano-Carrizales et al.,⁴⁰ that gives the analytical dependence of the dispersion D (defined as the number of surface atoms over the total number of atoms in cluster) versus the particle size m , holding for any fcc metal particle with perfect cuboctahedral shape:

$$D = N_{\text{surf}}/N_{\text{tot}} = (30m^2 + 6)/(10m^3 + 15m^2 + 11m + 3) \quad \text{with } m \text{ integer greater than } 0 \quad (1)$$

where m defines the particle size in terms of successive monoatomic crust added to a pre-existing core (i.e., particle with size $m - 1$). In such a way, $m = 0$ represents the isolated atom, $m = 1$ represents a 13 atom cluster where the central one has fully saturated its 12 coordinations, etc. To use eq 1 for determining the S/V_{TEM} for the Pd particle size distribution measured by TEM, we need a conversion from the d value in angstroms to the dimensionless m value. This relationship is linear and directly defined by the a lattice parameter of the fcc unit cell (or by the metal–metal first shell bond length). For palladium, the value of $a = 3.89$ Å ($R_{\text{Pd-Pd}} = 2.75$ Å) results in the d vs m relationship of $d(m) = 4.561m + 3.2$, reported as

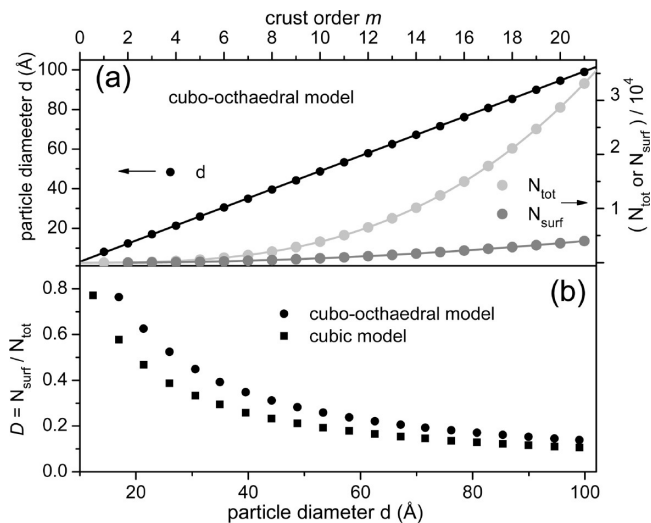


Figure 1. (a) Particle diameter d , total number of atoms N_{tot} , and number of surface atoms N_{surf} obtained as a function of the crust order m from the cuboctahedral geometrical model:^{39,40} $d(m) = 4.561m + 3.2$ (left ordinate axis); $N_{\text{tot}} = 10/3m^3 + 5m^2 + 11/3m + 1$; $N_{\text{surf}} = 10m^2 + 2$ (both right ordinate axis). $d(m)$ holds for palladium only, while $N_{\text{tot}}(m)$ and $N_{\text{surf}}(m)$ are general for all fcc metals. (b) Evolution of the dispersion as a function of the particle diameter for the cuboctahedral geometrical model^{39,40} (scattered circles). For comparison, the dispersion of a cubic cluster of size d is also reported (scattered squares).

black curve in Figure 1a, reporting also the evolution, as a function of m , of both the total number of atoms ($N_{\text{tot}}(m) = 10/3m^3 + 5m^2 + 11/3m + 1$) and the number of surface atoms ($N_{\text{surf}} = 10m^2 + 2$), from which eq 1 derives straightforwardly.

Figure 1b reports D values as a function of the particle diameter d , that are used to convert the size dispersion data into the S/V_{TEM} value according to eq 2:

$$S/V_{\text{TEM}} = \frac{5}{6} \frac{\sum_{i=1}^{N_{\text{particle}}} D(d_i) N_{\text{tot}}(d_i)}{\sum_{i=1}^{N_{\text{particle}}} N_{\text{tot}}(d_i)} \quad (2)$$

where N_{particle} is the number of particles investigated in the TEM study, larger than 200 in all cases. The reduction factor 5/6 represents an arbitrary way to take into account the fraction of the particle surface that, being in direct contact with the support, is not available for the gas adsorption processes. The so obtained S/V_{TEM} value will be compared to the S/V_{Chem} ones, independently evaluated from CO chemisorption. Note that the geometric shape assumed in this model is relevant to define the deduced $N_{\text{tot}}(d)$, $N_{\text{surf}}(d)$, and $D(d)$ trends on a quantitative ground. For comparison, Figure 1b also reports the D value obtained starting from a cubic particle (scattered squares). In the present case, the cuboctahedral shape of the particles is fully supported by the high resolution TEM investigation.

2.2.3. EXAFS. X-ray absorption experiments, at the Pd K-edge (24350 eV), were performed at the BM26A beamline of the ESRF facility (Grenoble, France). The white beam was monochromatized using a Si(111) double crystal; harmonic rejection has been performed using Pt-coated silicon mirrors. The following experimental geometry was adopted: (1) I_0 (10% efficiency); (2) sample; (3) I_1 (40% efficiency); (4) reference Pd foil; (5) I_2 (80% efficiency). This setup allows a direct energy/angle calibration for each spectrum, avoiding any problem related to small energy shifts due to small thermal instability of the monochromator crystals.⁴¹ The EXAFS part of the spectra were collected with a variable sampling step in energy, resulting in $\Delta k = 0.05 \text{ \AA}^{-1}$, up to 20 \AA^{-1} , with an

integration time that linearly increases with k from 4 to 25 s/point to account for the low signal-to-noise ratio at high k values. Samples, in the form of self-supported pellets of optimized thickness, have been located inside an ad hoc conceived cell that allows in situ evacuation, gas dosage, and warming and cooling.⁴²

The extraction of the $\chi(k)$ function has been performed using Athena code.⁴³ For each sample, two consecutive EXAFS spectra have been collected and corresponding $\chi(k)$ functions have been averaged before data analysis. EXAFS data analysis has been performed using the Arthemis software.⁴³ Phase and amplitudes have been calculated by FEFF6 code,⁴⁴ and have been successfully checked with Pd metal foil. For each sample, the averaged $k^3\chi(k)$ function were Fourier transformed in the $\Delta k = 2.00\text{--}15.75 \text{ \AA}^{-1}$ interval. The fits were performed in R -space in the $\Delta R = 1.00\text{--}3.01 \text{ \AA}$ range ($2\Delta k\Delta R/\pi > 17$). As recently demonstrated by the group of van Bokhoven,¹³ the standard EXAFS data analysis on small metal particles can be subjected to systematic errors in both coordination numbers and average distances. The magnitude of the error was particularly relevant for data collected at high temperature (673 K). This is due to the heterogeneity of the particles that results in a non-Gaussian distribution of distances, that is incorrectly fitted by an increase of the Debye–Waller factor of static origin. To overcome this problem, van Bokhoven et al.¹³ performed the EXAFS data analysis using the cumulant approach.^{45–49}

In this work, we perform only a first shell data analysis using both the standard and the cumulant approaches. In the cumulant approach, the third cumulant, c_3 , resulted in very small value ($c_3 \approx 5 \times 10^{-5}$, with a comparable or higher incertitude) and was unable to modify the other fit parameters, particularly the Pd–Pd first shell average distance. Conversely, the fourth cumulant, c_4 , correlates with the coordination number N (and thus with the average particle diameter $\langle d \rangle$; see the relationship reported in the inset of Figure 2b). The N values obtained with the two approaches are systematically different, those obtained with the standard approach being larger than those obtained in the cumulant approach by about 10%, i.e., by about one unit. After a carefully investigation of both set of results, we decided to consider as more reliable those obtained with the standard approach for the following reasons. (i) The incertitude associated with c_4 was 70–80% of the optimized value. (ii) By optimizing c_4 (N), in fits where N (c_4) has been fixed to slightly different values, the correlation between N and c_4 is opposite to what was expected from the literature:¹³ negative c_4 values resulted in a decrease of the N value, with respect to the fit obtained imposing $c_4 = 0$.

2.2.4. FTIR Spectroscopy. CO adsorption on the Pd nanoparticles has been investigated also by means of transmission FTIR measurements, performed on self-supported pellets inside an IR quartz cell suitable for thermal treatments in vacuum and/or controlled atmosphere. The samples have been heated up to the desired reduction temperature under dynamic vacuum. The reduction process consists of three subsequent H_2 dosages (equilibrium pressure $P_{\text{H}_2} = 120 \text{ Torr}$, $1 \text{ Torr} = 133.3 \text{ Pa}$, contact time = 5 min). H_2 was removed at the reduction temperature ($P_{\text{H}_2} < 10^{-4} \text{ Torr}$), and successively the samples were cooled to 300 K in a dynamical vacuum. This procedure allowed us to obtain the reduced sample in situ inside the IR cell. All the outgassed samples were then contacted in situ with CO ($P_{\text{CO}} = 50 \text{ Torr}$). The FTIR spectra were recorded at room temperature at 2 cm^{-1} resolution, using a Bruker IFS28 spectrometer, equipped with a cryogenic MCT detector. P_{CO} was then gradually reduced in steps from 50 to 10^{-4} Torr . After

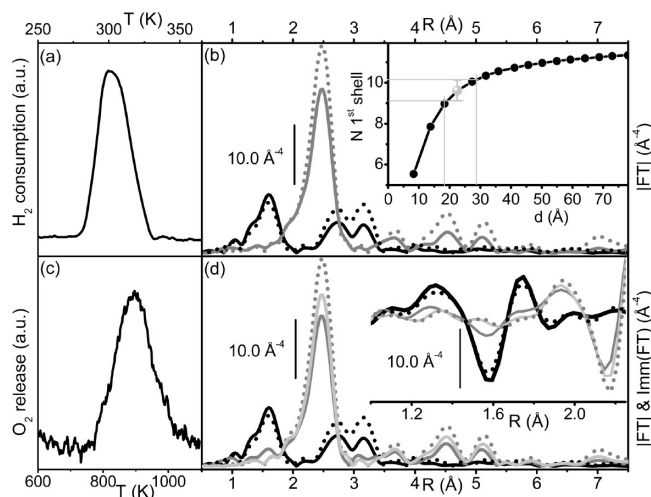


Figure 2. Top: H_2 reduction at 393 K of the Pd/SA sample as followed by TPR (part a) and EXAFS (part b). Initial Pd/SA sample: full black curve; H_2 -reduced at 393 K: full gray curve; metal Pd foil: dotted black curve; PdO model compound: black dotted curve. The inset reports the evolution of the average first shell Pd–Pd coordination number (N) for cuboctahedral Pd particles of increasing diameter obtained from the model reported elsewhere^{39,40} and summarized in Section 2.2.2. The optimized N value obtained in the fitting of the EXAFS data for the Pd/SA sample reduced in H_2 at 393 K is reported as gray dot, with the corresponding error bar (gray lines). Bottom: thermal decomposition of Pd/SA sample as followed by TPD (part c) and EXAFS (part d). Initial Pd/SA sample: full black curve; thermal decomposition at 673 and 823 K: dark and light gray curves; metal Pd foil: dotted gray curve. PdO model compound: black dotted curve. Both modulus (main part) and imaginary parts (inset) of the k^3 -weighted, phase-uncorrected, Fourier transform of the EXAFS spectra are reported.

each step, the FTIR spectrum of the remaining adsorbed CO species was acquired. The final spectrum corresponds to CO species irreversibly adsorbed at 300 K. All the spectra reported in this work have been normalized in order to take into account the different optical thicknesses of the samples, i.e., the quantity of Pd crossed by the IR beam. Consequently, along the whole set of samples, the apparent intensity of a given band is directly proportional to the amount of carbonyl species responsible for the component, so that all the spectra are directly comparable to each other.

3. Results and Discussion

3.1. PdO Deposition on the SA Support. The deposition of palladium hydroxide on the SA support has been previously investigated by means of N_2 adsorption measurements and SEM techniques.³⁷ It has been demonstrated that both the basicity of the solution used for the deposition of Pd from Na_2PdCl_4 and the final washing procedures cause non-negligible modifications in the pore texture of the support, that is partially dissolved. Conversely, high temperature activation treatments, either in air or H_2 atmosphere, on the Pd/SA system cause only modest changes in the pore texture of the support, that can be neglected in the following.

3.2. PdO H_2 -Reduction and Thermal Decomposition: Formation of the Pd Particles. TPR measurement (Figure 2a) shows that reduction of the Pd/SA sample in presence of H_2 starts already at 265 K and is completed at 335 K. The negative peak around 330 K, due to decomposition of Pd hydride phase,⁵⁰ is hardly visible, because the formation of the metal phase is not complete in the temperature range of Pd hydride stability. The integrated hydrogen consumption corresponds to a complete

$\text{Pd}^{2+} \rightarrow \text{Pd}^0$ reduction ($H_{\text{consumed}}/\text{Pd} = 1.99$, 2 being the theoretical value).

The complete reduction of Pd/SA upon treatment in H_2 is also demonstrated by EXAFS spectroscopy (Figure 2b). The spectrum of initial Pd/SA sample (full black curve) is typical of Pd^{2+} species, showing a first Pd–O shell at ~ 1.60 Å and two higher shell peaks at ~ 2.75 and ~ 3.15 Å (phase uncorrected values). These features, very similar to those observed in the case of the PdO reference compound (dotted black curve), and consistent with the analysis made by Troitskii et al.^{51,52} on Pd^{2+} -polynuclearhydroxo complexes, totally disappear in the sample H_2 -reduced at 393 K (gray curve), demonstrating a complete reduction to Pd^0 . The spectrum of the H_2 -reduced sample (gray curve) is characterized by the typical features of the Pd fcc system (see dotted gray curve): a first shell Pd–Pd peak at ~ 2.47 Å, and higher shell peaks at ~ 3.70 , 4.50, 5.15, and 5.90 Å. The only difference within these spectra concerns the peak intensity, reflecting a decrease in the average coordination number, as expected in the case of small Pd particles. This is confirmed also by the absence of the peak at 7.00 Å, observed only in the bulk case. Indeed, indirect information on the average particle size of the Pd metal particles can be obtained by EXAFS. The evolution of the average first shell Pd–Pd coordination number N versus increasing Pd particle diameter $\langle d \rangle$, computed for a cuboctahedral cluster, is reported in the inset of Figure 2b.^{39,40} The average Pd coordination number obtained by fitting the EXAFS spectrum of Pd/SA H_2 -reduced at 393 K is 9.9 ± 0.5 , vs 12 of the bulk, corresponding to an average particle diameter of $\langle d \rangle_{\text{EXAFS}} = 24.2$ Å. Due to the strongly asymmetric $\langle d \rangle$ vs N relationship reported in the inset of Figure 2b, the ± 0.5 error bar found for N implies an asymmetric propagation to $\langle d \rangle$, that ranges between 21 and 33 Å; see vertical gray lines.

$\text{Pd}^{2+} \rightarrow \text{Pd}^0$ reduction can also be achieved by thermal decomposition of the Pd/SA sample. TPD measurement (Figure 2c) shows that O_2 is released at high temperature, with a broad peak exhibiting a maximum around 900 K. The EXAFS spectra of the Pd/SA sample outgassed at high temperature demonstrate that PdO is progressively decomposed with the consequent formation of Pd^0 metal particles. The reduction is only partial at 673 K (Figure 2d, dark gray curve), as evident by looking at the imaginary parts of the FT (see inset), still showing in the 1.0–2.0 Å range the typical features of PdO. These features totally disappeared upon outgassing at 823 K (light gray curve), demonstrating complete PdO decomposition. The intensity of the first shell Pd–Pd signal is comparable to that obtained by reduction in H_2 at 393 K (gray curve in Figure 2b), suggesting that the two different treatments result in a comparable average Pd particle size. Note that TPD and EXAFS experiments are conducted in dynamic and static conditions, respectively. This explains why the complete PdO decomposition is achieved at slightly different temperatures in the two cases.

3.3. Pd Particle Size Distribution: TEM vs CO Chemisorption. Direct information on the particle size distribution has been obtained by a systematic TEM analysis on a statistically significant number of particles (see Experimental Section). Pd/SA samples H_2 -reduced at increasing temperatures exhibit a highly homogeneous dispersion of the metal particles on the support, as reported in Figure 3d. The relative particle size distribution, with the calculated mean size ($\langle d \rangle_{\text{TEM}}$) and standard deviation (σ), are reported in Figure 3a–c.

The particle size distribution of the Pd/SA sample reduced at 393 K is quite symmetric and narrow, as the diameter of most of the particles lies in the 20–40 Å range ($\langle d \rangle_{\text{TEM}} = 28$

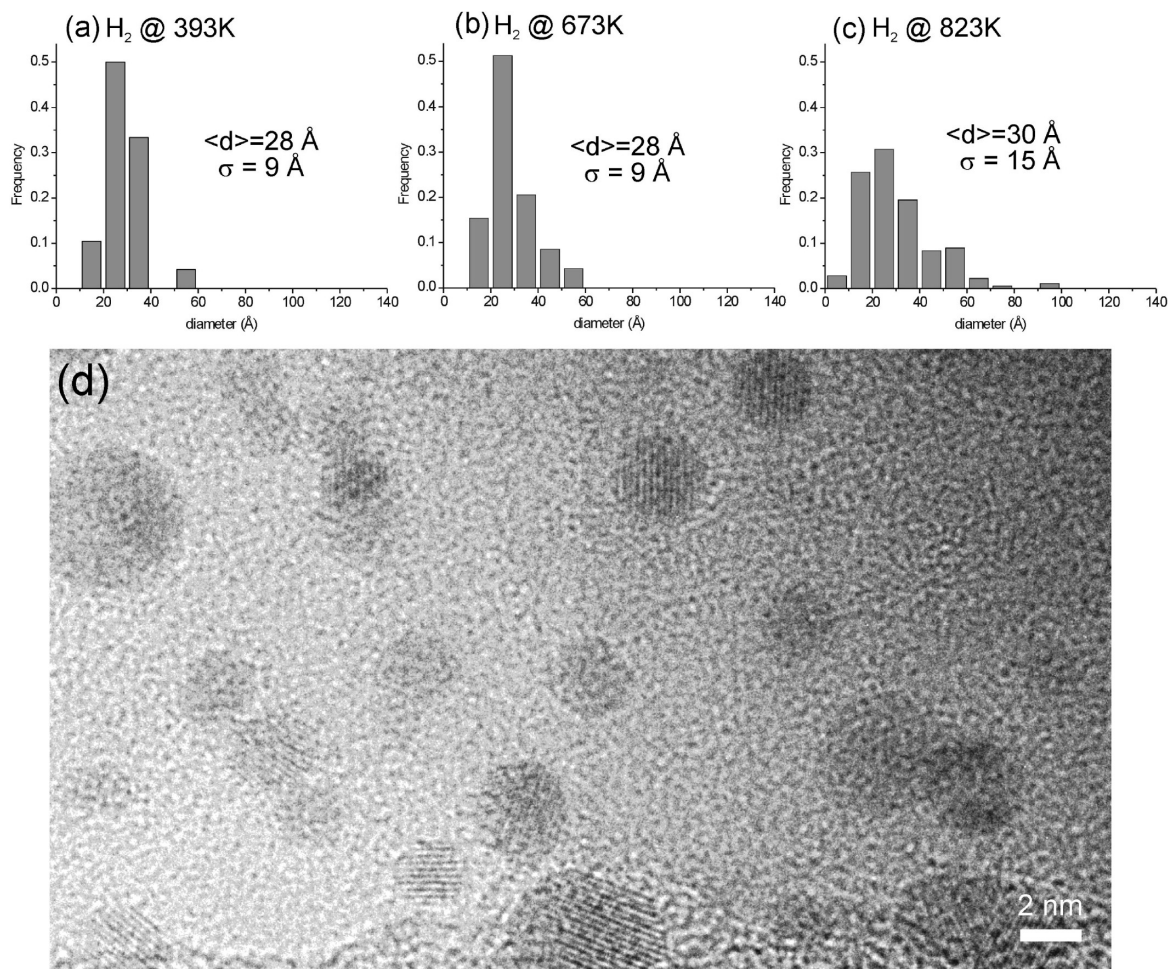


Figure 3. (a–c) Particle size distribution on the Pd/SA sample H₂-reduced at 393, 673, and 823 K, respectively. (d) High-resolution transmission electron micrograph of the Pd/SA sample reduced in H₂ at 673 K, showing the typical homogeneous dispersion of the metal particles on the support. Some particles are properly oriented with respect to the electron beam to show the typical interference fringes of Pd metal.

TABLE 2: Mean Particle Size ($\langle d \rangle_{\text{TEM}}$) and Surface/Volume Atom Ratio (S/V_{TEM}) As Obtained by TEM, Compared to the Surface/Volume Atom Ratio As Obtained by CO Chemisorption (S/V_{Chem})

H ₂ -reduction temperature (K)	$\langle d \rangle_{\text{TEM}}$ (Å)	S/V_{TEM} (%)	S/V_{Chem} (%)
393	27.9	29.2	28.2
673	28.4	28.8	21.1
823	29.9	24.2	12.4

Å, standard deviation of 9 Å). This value is slightly higher than the average $\langle d \rangle_{\text{EXAFS}} = 24.2 \text{ Å}$. However, the two values are comparable within the error bars ($\langle d \rangle_{\text{EXAFS}}$ in the 21–33 Å range). By increasing the reduction temperature, no significant variation of $\langle d \rangle_{\text{TEM}}$ is observed. However, a change of the shape of the distribution occurs: this change is minimal for the sample reduced in H₂ at 673 K and becomes relevant for that reduced at 823 K. In particular, we observe a decrease of the population in the 20–40 Å range and an overall broadening of the particle size distribution (Figure 3c), particularly relevant in the right side of the distribution, as a result of a moderate sintering process. From the particle size distributions reported in Figure 3a–c, the surface to volume ratio S/V_{TEM} has been calculated (i.e., the so-called “dispersion”, see eq 2 in the Experimental Section). From the S/V_{TEM} values reported in Table 2, the moderate sintering effect as a function of temperature is more evident than from bare $\langle d \rangle_{\text{TEM}}$.

The available surface area of dispersed Pd particles obtained by converting the crystal size distribution measured by TEM

into S/V_{TEM} ratio requires the assumption of a proper geometric model, that is a simplification of the true crystal shape (see Experimental Section). Moreover, TEM dispersion represents the potentially available surface Pd atoms, because, even at the surface, metal atoms are not available because of many phenomena (such as decoration, encapsulation, poisoning, or doping). The true available Pd surface atoms can be measured directly by means of chemisorption of proper molecules, that gives the dispersion, i.e., the ratio between surface and total metal atoms.⁴ Also this technique is not free from possible defects. In fact, it requires the knowledge of the average stoichiometry of the adsorbate–surface Pd adduct under the adopted experimental conditions. In this case a CO/Pd average stoichiometry = 1 has been adopted (see Experimental Section).

The true available Pd surface atoms (S/V_{Chem}) of the Pd/SA samples at different reduction temperatures are reported in Table 2 and compared with the potentially available Pd surface atoms (S/V_{TEM}). For Pd/SA sample reduced at 393 K, $S/V_{\text{Chem}} \cong S/V_{\text{TEM}}$. The agreement between TEM and CO chemisorption data does not hold on the sample reduced at 673 K, where CO chemisorption reveals a significant decrease of S/V_{Chem} ratio (close to 25%), while S/V_{TEM} is almost unchanged. The discrepancy between the two techniques becomes even more striking for the Pd/SA sample reduced at 823 K, where S/V_{Chem} decreases by 55%, whereas S/V_{TEM} shows only a small decrease of less than 10%, already explained in terms of moderate sintering. This means that a progressively increasing fraction

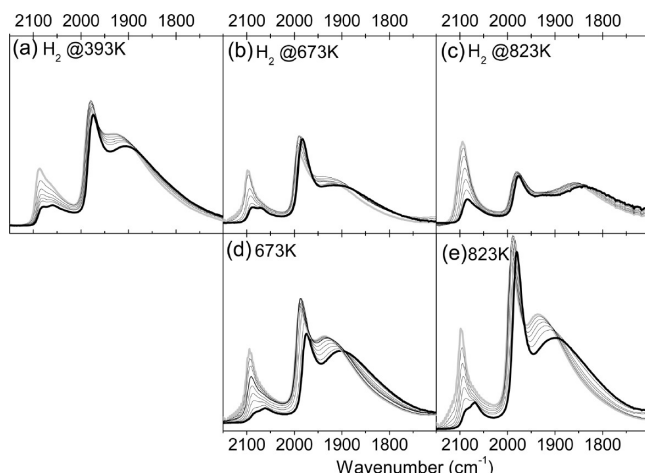


Figure 4. FTIR spectra of CO dosed at RT on the Pd/SA sample subjected to different activation procedures: H₂-reduction at increasing temperature (parts a–c), and thermal decomposition at 673 and 823 K (parts d and e, respectively). The sequences of spectra show the effect of decreasing P_{CO} , from 50 (bold gray curve) to 10^{−4} Torr (bold black curve).

of Pd surface sites becomes unavailable for CO adsorption upon increasing the reduction temperature. Having previously demonstrated the stability of the support under the adopted experimental conditions,³⁷ the more reasonable hypothesis to justify the experimental data is an important poisoning of the potentially available Pd surface during high temperature H₂-reduction processes. Conversely, when the reduction of Pd/SA sample is achieved by thermal decomposition at high temperature, the S/V_{Chem} ratio remains almost unchanged (29.7% and 29.0% for the sample calcined at 673 and 823 K, respectively). These data undoubtedly confirm the role played by H₂ in determining the poisoning of the Pd surface. However, neither TEM nor CO chemisorption can be informative on the nature of the species poisoning the Pd surface. To shed light on this point, FTIR spectroscopy of the adsorbed CO probe has been used.^{53–56}

3.4. Characterization of the Available Pd Surface by FTIR Spectroscopy of Adsorbed CO. FTIR spectroscopy of adsorbed CO is an efficient technique to obtain information on the exposed faces of supported metal nanoparticles and on their defectivity.^{2,12,25,57–65} We have recently demonstrated that it is possible to compare the results obtained on polycrystalline supported systems with those obtained on single crystals, thus bridging the gap between surface science and catalysis.²⁵ In this work, CO is adopted to probe the nature of the surface sites in order to obtain information directly comparable to those obtained by CO chemisorption measurements.

Figure 4 reports the FTIR spectra of CO dosed at 300 K on the Pd/SA sample H₂-reduced (parts a–c) and outgassed (parts d and e) at increasing temperature, upon decreasing coverage (θ). In our experimental conditions, θ_{max} (bold gray curve) corresponds to $T = 300$ K and $P_{\text{CO}} = 50$ Torr, whereas θ_{min} (bold black curve) is obtained by evacuation at 300 K down to 10^{−4} Torr. In all the parts, three main components are clearly evident, easily assigned on the basis of the surface science literature,^{1,3,20–24,57,61,62,66–74} from high to low $\tilde{\nu}(\text{CO})$, to (i) linear carbonyls on Pd(111) faces and/or on defects; (ii) 2-fold bridged carbonyls on Pd(100) faces; (iii) 2-fold bridged carbonyls on Pd(111) faces. These three components will be labeled in the following as I, II, and III, respectively. Three-fold bridged carbonyls on Pd(111) faces are not observed in the reported spectra because, owing to the strong CO/Pd interaction, the

TABLE 3: $\tilde{\nu}(\text{CO})$ (in cm^{−1}) of the Different Types of Carbonyls Formed on Pd(111) and Pd(100) Faces of Pd/SA Subjected to Different Activation Procedures^a

band	H ₂			vacuo	
	393K	673K	823K	673K	823K
Ia	2088/2080	2097/2088	2094/2085	2096/2084	2097/2087
Ib	2060/2060	2065/2065	2060/2060	2061/2061	2065/2065
II	1980/1974	1994/1984	1980/1980	1988/1974	1992/1980
III	1928/1905	1933/1905	1864/1841	1936/1900	1934/1900

^a The bands are labeled I, II, and III according to the text, while boldface and lightface values refer to the highest and lowest coverages explored in the work, respectively, corresponding to the bold gray and bold black spectra reported in Figure 4.

lowest CO coverage cannot be reached by evacuation at RT down to 10^{−4} Torr.²⁵

The sample reduced in H₂ at 393 K (Figure 4a) shows the typical spectrum expected for Pd particles exposing both (111) and (100) faces. The positions of the three main components are described in Table 3 as a function of the coverage. It is worth noticing that band I (due to linear carbonyls formed on (111) faces) is clearly double, with a maximum at 2088 cm^{−1} that progressively downward shifts at 2080 cm^{−1} upon decreasing θ , and a well-defined shoulder at 2060 cm^{−1}, that remains almost unchanged, both in intensity and frequency position, upon lowering the coverage. These two components, labeled as Ia and Ib in Table 3, are assigned to linear carbonyls formed on exposed (111) faces and on defects, respectively.^{19,25,63,64,69} Upon increasing the reduction temperature to 823 K (Figure 4b,c), gradual changes occur. In particular: (i) band II decreases in intensity; (ii) the relative ratio between band I and band III is reversed; (iii) an important red-shift of band III is observed, in particular for the sample reduced at 823 K ($\Delta\tilde{\nu} \sim -60$ cm^{−1}, see Table 3). These changes may be explained with two main hypotheses: (i) a relevant change in the Pd particles morphology or (ii) a poisoning of the exposed surfaces. Hypothesis (i) seems unrealistic on the basis of the TEM measurements, that do not demonstrate a change in the shape of the Pd particles. Moreover, a change in the Pd particle morphology would not help to explain the red-shift of band III. Therefore, a poisoning of the exposed surfaces has to be considered, in agreement with the hypothesis already advanced to explain the CO chemisorption experiments. The poisoning species (having a molecular character) should occupy the same sites of a bridged CO molecule, so that the incoming CO molecules arrange themselves preferentially in a linear way. Note that at low θ the spectra are more similar to the standard ones. This interpretation also explains the red-shift of band III, because the poisoning of the exposed adsorption sites does not allow the coupling of the CO oscillators to be fully operative.²⁵

In order to define the nature of the poisoning species, FTIR spectroscopy of adsorbed CO has been applied to Pd/SA samples subjected to thermal reduction at 673 K (Figure 4d) and 823 K (Figure 4e). The corresponding FTIR spectra, characterized by the standard components expected for Pd particles exposing both (111) and (100) faces, are the evidence of well-defined Pd particles characterized by very clean surfaces. These results indicate that, already at 673 K, PdO is decomposed to Pd also in absence of H₂. This result is in qualitative agreement with TPD (showing O₂ release with a maximum around 900 K; see Section 3.2), EXAFS (revealing that supported PdO is completely decomposed to metal Pd at 823 K, see Section 3.2), and CO chemisorption data (the Pd/SA sample calcined at 823 K shows the same dispersion as the sample H₂-reduced at 393 K;

see Section 3.3). Note that EXAFS analysis revealed that the PdO decomposition was not complete on the sample activated at 673 K, whereas in the FTIR spectra there is no evidence of Pd²⁺ species. This discrepancy can be, however, explained by considering that the residual PdO can be inside the core of the particle and thus not accessible to the CO probe.

Furthermore, by comparing the FTIR spectra obtained on the sample reduced in H₂ at 823 K (part c) with those obtained on the sample activated at the same temperature without H₂ (part e), it is clear that the previously discussed sample modification occurring by passing from 393 to 823 K is observed only in presence of H₂. We therefore hypothesize that the poisoning species are present in the support and they are extracted only in the presence of H₂. Among the possibilities, we have identified three candidates, all present in the support as impurities or arising from raw materials (see Section 2.1).

(a) Sulfur is the best candidate because (i) it is a well-known poison of noble metals,^{75–81} (ii) it is present as “inert” sulfate in the support, that is reduced by H₂ to poisonous H₂S (in air the process does not occur), (iii) very small amounts of S are sufficient to significantly poison the Pd surface (0.2 wt.% is sufficient to form a surface stoichiometry S/Pd_{surf} = 1/1, but a much lower ratio is sufficient to deeply change the Pd surface). This is an important feature because poison must be present in a low amount on the Pd surface, not being detectable by EXAFS. In this respect, note that the 0.08% S content revealed by XRF (see Experimental Section) should be sufficient to poison a relevant fraction of the surface, especially considering that it has a great affinity toward noble metals such as Pd.

(b) Chlorine, a residual presence that arises from Pd raw material or already present as an impurity in the carrier, is a known poison similar to sulfur⁸¹ and can be mobilized from the support in the form of HCl. During thermal treatments up to 823 K, a great amount of H₂O is released from the support³⁷ and, in a much less amount, from reduction of PdO. This H₂O should be responsible for the mobilization of chlorine from the support or from PdO itself in the form of HCl. We can recall here that thermal release from chlorinated oxides occurs through [Me–Cl] + [HO–Me] → [Me–O–Me] + HCl reaction in the case of alumina or silica^{82–87} or does not occur at all in the case of alkali and alkali earth metal chlorides (even in the presence of H₂). Consequently, the effect of chlorine should also be detectable by heating in air, opposite to what was observed.

(c) Ca poisoning has been claimed by Prins et al.,⁸⁸ but in our case, this choice does not explain the determining effect of H₂.

On these bases, sulfur seems to be the most reliable source of poisoning, even if from the whole set of data the presence of other poisoning species cannot be completely discarded.

4. Conclusions

In this work we followed the reducibility, sintering, and surface properties of Pd metal nanoparticles deposited on a peculiar high surface area SiO₂–Al₂O₃ (SA) support as a function of the activation temperature and activation atmosphere (with or without H₂). An accurate TEM study allowed us to determine the Pd particle size distribution and the cuboctahedral-like shape of the metal particles. By adopting the geometrical models present in the literature,^{39,40} we have been able to extract from the Pd particle size distribution both (i) the average Pd–Pd first shell coordination number (*N*_{Pd}), to be compared with parallel EXAFS study, and (ii) the fraction of surface Pd atoms, to be compared with the dispersion measured by CO chemisorption. The *S/V*_{Chem} value decreases significantly upon

increasing the H₂ reduction temperature. According to TEM, the sintering process can only account for a very small fraction of the *S/V*_{Chem} decrease, suggesting important poisoning of the potentially available Pd surface. This hypothesis is supported by a parallel experiment of thermal decomposition at the same temperature (in absence of H₂), showing that the *S/V*_{Chem} value is almost unchanged. FTIR spectroscopy of adsorbed CO allowed us to probe the nature of the Pd surface available for adsorption and to confirm the hypothesis.

Acknowledgment. We are indebted to the whole staff of BM26 DOUBBLE beamline, and to S. Nikitenko in particular, for the competent and friendly support during the Pd K-edge X-ray absorption experiment (Proposal CH-2350). We are also indebted to Massimo Graziani (Chimet S.p.A.) for the CO chemisorption measurements.

References and Notes

- Freund, H. J. *Angew. Chem., Int. Ed. Engl.* **1997**, *36*, 452.
- van der Eerden, A. M. J.; Visser, T.; Nijhuis, A.; Ikeda, Y.; Lepage, M.; Koningsberger, D. C.; Weckhuysen, B. M. *J. Am. Chem. Soc.* **2005**, *127*, 3272.
- Henry, C. R. *Surf. Sci. Rep.* **1998**, *31*, 235.
- Berthoud, R.; Delichère, P.; Gajan, D.; Lukens, W.; Pelzer, K.; Basset, J.-M.; Candy, J.-P.; Copéret, C. *J. Catal.* **2008**, *260*, 387.
- Vogel, W.; Knozinger, H.; Carvill, B. T.; Sachtler, W. M. H.; Zhang, Z. C. *J. Phys. Chem. B* **1998**, *102*, 1750.
- Frenkel, A. I. *J. Synchrotron Radiat.* **1999**, *6*, 293.
- Alexeev, O.; Gates, B. C. *Top. Catal.* **2000**, *10*, 273.
- (a) Frenkel, A. I.; Hills, C. W.; Nuzzo, R. G. *J. Phys. Chem. B* **2001**, *105*, 12689. (b) Sergio, I.; Sanchez, S. I.; Menard, L. D.; Ariella, A.; Kang, J. H.; Small, M. W.; Nuzzo, R. G.; Frenkel, A. I. *J. Am. Chem. Soc.* **2009**, *131*, DOI: 10.1021/ja809182v.
- Guzman, J.; Gates, B. C. *Angew. Chem., Int. Ed.* **2003**, *42*, 690.
- Sun, Y.; Frenkel, A. I.; Isseroff, R.; Shonbrun, C.; Forman, M.; Shin, K. W.; Koga, T.; White, H.; Zhang, L. H.; Zhu, Y. M.; Rafailovich, M. H.; Sokolov, J. C. *Langmuir* **2006**, *22*, 807.
- Carlsson, A.; Puig-Molina, A.; Janssens, T. V. W. *J. Phys. Chem. B* **2006**, *110*, 5286.
- Bertarione, S.; Prestipino, C.; Groppo, E.; Scarano, D.; Spoto, G.; Zecchina, A.; Pellegrini, R.; Leofanti, G.; Lamberti, C. *Phys. Chem. Chem. Phys.* **2006**, *8*, 3676.
- Bus, E.; Miller, J. T.; Kropf, A. J.; Prins, R.; van Bokhoven, J. A. *Phys. Chem. Chem. Phys.* **2006**, *8*, 3248.
- Rotunno, F.; Prestipino, C.; Bertarione, S.; Groppo, E.; Scarano, D.; Zecchina, A.; Pellegrini, R.; Leofanti, G.; Lamberti, C. *Stud. Surf. Sci. Catal.* **2006**, *162*, 721.
- Knecht, M. R.; Weir, M. G.; Frenkel, A. I.; Crooks, R. M. *Chem. Mater.* **2008**, *20*, 1019.
- Newton, M. A. *Chem. Soc. Rev.* **2008**, *37*, 2644.
- Liotta, L. F.; Deganello, G.; Delichère, P.; Leclercq, C.; Martin, G. A. *J. Catal.* **1996**, *164*, 334.
- Hoffmann, F. M. *Surf. Sci. Rep.* **1983**, *3*, 107.
- Hollins, P. *Surf. Sci. Rep.* **1992**, *16*, 51.
- Xu, X. P.; Goodman, D. W. *J. Phys. Chem.* **1993**, *97*, 7711.
- Xu, X. P.; Chen, P. J.; Goodman, D. W. *J. Phys. Chem.* **1994**, *98*, 9242.
- Wolter, K.; Seifert, O.; Libuda, J.; Kuhlbeck, H.; Baumer, M.; Freund, H. J. *Chem. Phys. Lett.* **1997**, *277*, 513.
- Wolter, K.; Seifert, O.; Libuda, J.; Kuhlbeck, H.; Baumer, M.; Freund, H. J. *Surf. Sci.* **1998**, *404*, 428.
- Freund, H. J.; Baumer, M.; Kuhlbeck, H. *Adv. Catal.* **2000**, *45*, 333.
- Groppo, E.; Bertarione, S.; Rotunno, F.; Agostini, G.; Scarano, D.; Pellegrini, R.; Leofanti, G.; Zecchina, A.; Lamberti, C. *J. Phys. Chem. C* **2007**, *111*, 7021, and references therein.
- Rylander, P. N. *Catalytic Hydrogenation in Organic Syntheses*; Academic Press, Inc.: New York, 1979.
- Blaser, H. U.; Indolese, A.; Schnyder, A.; Steiner, H.; Studer, M. *J. Mol. Catal. A: Chem.* **2001**, *173*, 3.
- Kneipp, K.; Kneipp, H.; Itzkan, I.; Dasari, R. R.; Feld, M. S. *Chem. Rev.* **1999**, *99*, 2957.
- Link, S.; El-Sayed, M. A. *J. Phys. Chem. B* **1999**, *103*, 8410.
- Sun, Y. G.; Xia, Y. N. *Science* **2002**, *298*, 2176.
- Kelly, K. L.; Coronado, E.; Zhao, L. L.; Schatz, G. C. *J. Phys. Chem. B* **2003**, *107*, 668.
- Damin, A.; Usseglio, S.; Agostini, G.; Bordiga, S.; Zecchina, A. *J. Phys. Chem. C* **2008**, *112*, 4932.

- (33) Kamat, P. V. *J. Phys. Chem. B* **2002**, *106*, 7729.
- (34) Agostini, A.; Usseglio, S.; Groppo, E.; Uddin, M. J.; Prestipino, C.; Bordiga, S.; Zecchina, A.; Solari, P. L.; Lamberti, C. *Chem. Mater.* **2009**, *21*, 1343.
- (35) Geus, J. W.; van Dillen, A. J. Preparation of supported catalysts by deposition-precipitation. In *Handbook of Heterogeneous Catalysis*; Ertl, G. K. H.; Weitkamp, J., Eds.; Wiley-VCH: Weinheim, 1997; Vol. 1, p 240.
- (36) Simonov, P. A.; Likhonolobov, V. A. Physicochemical Aspects of Preparation of Carbon-Supported Noble Metal Catalysts. In *Catalysis and Electrocatalysis at Nanoparticle Surfaces*; Wieckowski, A.; Savinova, E. R.; Vayenas, C. G., Eds.; Marcel Dekker, Inc.: New York, 2003; p 409.
- (37) Pellegrini, R.; Leofanti, G.; Agostini, G.; Rivallain, M.; Groppo, E.; Lamberti, C. *Langmuir* **2009**, *25*, 6476.
- (38) Prelazzi, G.; Cerboni, M.; Leofanti, G. *J. Catal.* **1999**, *181*, 73.
- (39) Fritzsche, H. G.; Benfield, R. E. *Z. Phys. D: At. Mol. Clusters* **1993**, *26*, S15.
- (40) Montejano-Carrizales, J. M.; Aguilera-Granja, F.; Moran-Lopez, J. L. *Nanostruct. Mater.* **1997**, *8*, 269.
- (41) Lamberti, C.; Bordiga, S.; Bonino, F.; Prestipino, C.; Berlier, G.; Capello, L.; D'Acapito, F.; Xamena, F.; Zecchina, A. *Phys. Chem. Chem. Phys.* **2003**, *5*, 4502.
- (42) Lamberti, C.; Prestipino, C.; Bordiga, S.; Berlier, G.; Spoto, G.; Zecchina, A.; Laloni, A.; La Manna, F.; D'Anca, F.; Felici, R.; D'Acapito, F.; Roy, P. *Nucl. Instrum. Methods B* **2003**, *200*, 196.
- (43) Ravel, B.; Newville, M. *J. Synchrotron Radiat.* **2005**, *12*, 537.
- (44) Ankudinov, A. L.; Ravel, B.; Rehr, J. J.; Conradson, S. D. *Phys. Rev. B* **1998**, *58*, 7565.
- (45) Dalba, G.; Fornasini, P.; Rocca, F. *Phys. Rev. B* **1993**, *47*, 8502.
- (46) Dalba, G.; Fornasini, P. *J. Synchrotron Radiat.* **1997**, *4*, 243.
- (47) Katsumata, H.; Miyanaga, T.; Yokoyama, T.; Fujikawa, T.; Ohta, T. *J. Synchrotron Radiat.* **2001**, *8*, 226.
- (48) Beccara, S. A.; Dalba, G.; Fornasini, P.; Grisenti, R.; Sanson, A. *Phys. Rev. Lett.* **2002**, *89*, xxx.
- (49) Fornasini, P.; Beccara, S. A.; Dalba, G.; Grisenti, R.; Sanson, A.; Vaccari, M.; Rocca, F. *Phys. Rev. B* **2004**, *70*, xxx.
- (50) Aben, P. C. *J. Catal.* **1968**, *10*, 224.
- (51) Troitskii, S. Y.; Chuvilin, A. L.; Kochubei, D. I.; Novgorodov, B. N.; Kolomiichuk, V. N.; Likhonolobov, V. A. *Russ. Chem. Bull.* **1995**, *44*, 1822.
- (52) Troitskii, S. Y.; Chuvilin, A. L.; Bogdanov, S. V.; Moroz, E. M.; Likhonolobov, V. A. *Russ. Chem. Bull.* **1996**, *45*, 1296.
- (53) Knözinger, H. Infrared spectroscopy for the characterization of surface acidity and basicity. In *Handbook of Heterogeneous Catalysis*; Ertl, G.; Knözinger, H.; Weitkamp, J., Eds.; Wiley-VCH: Weinheim, 1997; Vol. 2, p 707.
- (54) Zecchina, A.; Scarano, D.; Bordiga, S.; Spoto, G.; Lamberti, C. *Adv. Catal.* **2001**, *46*, 265.
- (55) Spoto, G.; Gribov, E. N.; Ricchiardi, G.; Damin, A.; Scarano, D.; Bordiga, S.; Lamberti, C.; Zecchina, A. *Prog. Surf. Sci.* **2004**, *76*, 71.
- (56) Lamberti, C.; Groppo, E.; Spoto, G.; Bordiga, S.; Zecchina, A. *Adv. Catal.* **2007**, *51*, 1.
- (57) Tessier, D.; Rakai, A.; Bozonverduraz, F. *J. Chem. Soc., Faraday Trans.* **1992**, *88*, 741.
- (58) Craciun, R.; Daniell, W.; Knozinger, H. *Appl. Catal., A* **2002**, *230*, 153.
- (59) Pestryakov, A. N.; Lunin, V. V.; Fuentes, S.; Bogdanchikova, N.; Barrera, A. *Chem. Phys. Lett.* **2003**, *367*, 102.
- (60) Skotak, M.; Karpinski, Z.; Juszczak, W.; Pielaszek, J.; Kepinski, L.; Kazachkin, D. V.; Kovalchuk, V. I.; d'Itri, J. L. *J. Catal.* **2004**, *227*, 11.
- (61) Bertarione, S.; Scarano, D.; Zecchina, A.; Johanek, V.; Hoffmann, J.; Schauermaun, S.; Frank, M. M.; Libuda, J.; Ruppachter, G.; Freund, H. J. *J. Phys. Chem. B* **2004**, *108*, 3603.
- (62) Lear, T.; Marshall, R.; Gibson, E. K.; Schutt, T.; Klapotke, T. M.; Ruppachter, G.; Freund, H. J.; Winfield, J. M.; Lennon, D. *Phys. Chem. Chem. Phys.* **2005**, *7*, 565.
- (63) Lear, T.; Marshall, R.; Lopez-Sanchez, J. A.; Jackson, S. D.; Klapotke, T. M.; Baumer, M.; Ruppachter, G.; Freund, H. J.; Lennon, D. *J. Chem. Phys.* **2005**, *123*, 174706.
- (64) Lear, T.; Marshall, R.; Lopez-Sanchez, J. A.; Jackson, S. D.; Klapotke, T. M.; Baumer, M.; Ruppachter, G.; Freund, H. J.; Lennon, D. *J. Chem. Phys.* **2006**, *124*, 69901.
- (65) Bollmann, L.; Ratts, J. L.; Joshi, A. M.; Williams, W. D.; Pazmino, J.; Joshi, Y. V.; Miller, J. T.; Kropf, A. J.; Delgass, W. N.; Ribeiro, F. H. *J. Catal.* **2008**, *257*, 43.
- (66) Wolter, K.; Seiferth, O.; Kuhlenbeck, H.; Bäumer, M.; Freund, H. J. *Surf. Sci.* **1998**, *399*, 190.
- (67) Surnev, S.; Sock, M.; Ramsey, M. G.; Netzer, F. P.; Wiklund, M.; Borg, M.; Andersen, J. N. *Surf. Sci.* **2000**, *470*, 171.
- (68) Sheppard, N.; De La Cruz, C. *Catal. Today* **2001**, *70*, 3.
- (69) Ozensoy, E.; Goodman, D. W. *Phys. Chem. Chem. Phys.* **2004**, *6*, 3765.
- (70) Henrich, V. E. *Rep. Prog. Phys.* **1985**, *48*, 1481.
- (71) Henrich, V. E.; Cox, P. A. *The Surface Science of Metal Oxides*; Cambridge University Press: Cambridge, 1994.
- (72) Barteau, M. A. *Chem. Rev.* **1996**, *96*, 1413.
- (73) Barteau, M. A.; Vohs, J. M., *Oxide model systems*, in: *Handbook of Heterogeneous Catalysis*; Ertl, G.; Knözinger, H.; Weitkamp, J., Ed.; Wiley-VCH: Weinheim, 1997; Vol. 2, p 873.
- (74) Xu, C.; Goodman, D. W. Ultrathin oxide films: model catalyst supports. In *Handbook of Heterogeneous Catalysis*; Ertl, G.; Knözinger, H.; Weitkamp, J., Ed.; Wiley-VCH: Weinheim, 1997; Vol. 2, p 826.
- (75) Wassmuth, H. W.; Ahner, J.; Hofer, M.; Stolz, H. *Prog. Surf. Sci.* **1993**, *42*, 257.
- (76) Feuerriegel, U.; Klose, W.; Sloboshanin, S.; Goebel, H.; Schaefer, J. A. *Langmuir* **1994**, *10*, 3567.
- (77) Gravi, P. A.; Toulhoat, H. *Surf. Sci.* **1999**, *430*, 176.
- (78) Hu, L. J.; Xia, G. F.; Qu, L. L.; Li, M. F.; Li, C.; Xin, Q.; Li, D. D. *J. Catal.* **2001**, *202*, 220.
- (79) Munakata, N.; Reinhard, M. *Appl. Catal., B* **2007**, *75*, 1.
- (80) Mori, A.; Mizusaki, T.; Kawase, M.; Maegawa, T.; Monguchi, Y.; Takao, S.; Takagi, Y.; Sajiki, H. *Adv. Synth. Catal.* **2008**, *350*, 406.
- (81) Bartholomew, C. H. *Appl. Catal., A* **2001**, *212*, 17.
- (82) Kytokivi, A.; Lindblad, M.; Root, A. *J. Chem. Soc., Faraday Trans.* **1995**, *91*, 941.
- (83) Leofanti, G.; Padovan, M.; Garilli, M.; Carmello, D.; Zecchina, A.; Spoto, G.; Bordiga, S.; Turnes Palomino, G.; Lamberti, C. *J. Catal.* **2000**, *189*, 91.
- (84) Leofanti, G.; Padovan, M.; Garilli, M.; Carmello, D.; Marra, G. L.; Zecchina, A.; Spoto, G.; Bordiga, S.; Lamberti, C. *J. Catal.* **2000**, *189*, 105.
- (85) Leofanti, G.; Marsella, A.; Cremaschi, B.; Garilli, M.; Zecchina, A.; Spoto, G.; Bordiga, S.; Fiscaro, P.; Berlier, G.; Prestipino, C.; Casali, G.; Lamberti, C. *J. Catal.* **2001**, *202*, 279.
- (86) Leofanti, G.; Marsella, A.; Cremaschi, B.; Garilli, M.; Zecchina, A.; Spoto, G.; Bordiga, S.; Fiscaro, P.; Prestipino, C.; Villain, F.; Lamberti, C. *J. Catal.* **2002**, *205*, 375.
- (87) Prestipino, C.; Bordiga, S.; Lamberti, C.; Vidotto, S.; Garilli, M.; Cremaschi, B.; Marsella, A.; Leofanti, G.; Fiscaro, P.; Spoto, G.; Zecchina, A. *J. Phys. Chem. B* **2003**, *107*, 5022.
- (88) Gusovius, A. F.; Watling, T. C.; Prins, R. *Appl. Catal., A* **1999**, *188*, 187.